

Natural cobalt–manganese oxide nanoparticles: speciation, detection and implications for cobalt cycling

Owen P. Missen^{A,B,*} , Stuart J. Mills^A, Thebny Thaise Moro^{C,D}, E. Eduardo Villalobos-Portillo^{E,G} , Hiram Castillo-Michel^E, Thomas E. Lockwood^F , Raquel Gonzalez de Vega^C and David Clases^C

Environmental context. Cobalt is a technologically critical element due to its uses in the green energy transition, but its cycling is poorly constrained in surface environments. We determined the form of cobalt in naturally enriched soils and found that it is commonly associated with manganese as mixed oxide nanoparticles. These findings demonstrate that the behaviour of critical elements such as cobalt in the environment is in part governed at the nanoscale.

For full list of author affiliations and declarations see end of paper

***Correspondence to:**

Owen P. Missen
Centre for Ore Deposit and Earth Sciences,
University of Tasmania, Private Bag 79,
Hobart, Tas. 7001, Australia
Email: owen.missen@utas.edu.au

Handling Editor:

Kevin Wilkinson

Received: 26 September 2023

Accepted: 14 February 2024

Published: 15 March 2024

Cite this: Missen OP *et al.* (2024) Natural cobalt–manganese oxide nanoparticles: speciation, detection and implications for cobalt cycling. *Environmental Chemistry* 21, EN23093. doi:10.1071/EN23093

© 2024 The Author(s) (or their employer(s)).
Published by CSIRO Publishing.

This is an open access article distributed under the Creative Commons Attribution-NonCommercial-NoDerivatives 4.0 International License (CC BY-NC-ND)

OPEN ACCESS

ABSTRACT

Rationale. Cobalt (Co) faces increasing demand for use in batteries and alloys, but its environmental behaviour in terrestrial surface environments is poorly constrained. This study analyses cobalt regolith mineralogy and nanoparticulate phase transitions to address this knowledge gap. **Methodology.** We studied Co-enriched environments across six localities and four distinct deposit types in arid and semi-arid Australian regolith environments to analyse its environmental behaviour. We used a combination of single particle inductively coupled plasma–mass spectrometry (SP ICP-MS) and synchrotron X-ray techniques (fluorescence microscopy, X-ray fluorescence microscopy and X-ray absorption spectroscopy). **Results.** We discovered the presence of Co oxide-based nanoparticles in soils surrounding cobalt-rich rocks at all of our studied locations, to our knowledge the first detection of terrestrial Co oxide-based nanoparticles. The extractable concentration of Co in the nanoparticles varied from 0.7 ng of nanoparticulate Co per gram of soil (ng Co g⁻¹), up to 1390 ng Co g⁻¹, the latter soil containing 1 × 10⁹ extractable Co-based nanoparticles per gram of soil. **Discussion.** Nanoparticulate cobalt was typically closely associated with manganese (Mn) in the form of natural Co–Mn oxide phases, with only two of the studied locations not showing a close Co–Mn association. We discuss the environmental drivers that may facilitate formation of Co–Mn oxide nanoparticles. Our study suggests that Co may be more mobile in surface environments than previously thought, with Co–Mn oxide nanoparticles found around all four analysed types of Co-rich outcrops.

Keywords: analytical chemistry, cobalt, critical element, earth chemistry, elemental cycling, manganese, metals, nanomaterials (natural), soil chemistry.

Introduction

Cobalt (chemical symbol Co, atomic number $Z = 27$) is a technologically critical element, indispensable for a green energy transition (Nansai *et al.* 2014; Watari *et al.* 2020; McNulty and Jowitt 2021). The growing demand for Co outstrips supply, a problem compounded by cobalt's complex chemical and geometallurgical behaviour (Dehaine *et al.* 2021; Pell *et al.* 2021; Whitworth *et al.* 2022). Additionally, large companies that manufacture Co-containing products are under considerable pressure to ensure that their Co supply chains are not profiting from exploitative labour conditions (Banza Lubaba Nkulu *et al.* 2018; Calvão *et al.* 2021; Mancini *et al.* 2021). Coupled to the complicated Co supply chain is the lack of knowledge surrounding its biogeochemical behaviour in terrestrial surface environments (Newsome *et al.* 2020), especially when compared to its better-studied oceanic cycling (Tagliabue *et al.* 2018; Chmiel *et al.* 2022). Increasing human exposure to Co is occurring directly as a result of mining, especially artisanal

mining, leading to higher blood levels of inorganic Co, as well as a higher incidence of respiratory issues (Banza Lubaba Nkulu *et al.* 2009; Musa Obadia *et al.* 2018; Schwartz *et al.* 2021; Muimba-Kankolongo *et al.* 2022). Disposal and recycling of Co-containing products such as batteries are also increasing the background concentrations of Co, although to what extent is not well quantified (Chandra *et al.* 2022; Huang 2023; Ma *et al.* 2023).

The movement of Co through terrestrial environments is tied to certain elements, particularly fellow transition metals such as Mn, Fe and Ni, especially in lateritic deposits (Friedrich *et al.* 2011; Newsome *et al.* 2020). S and As are together found in three quarters of all described Co minerals, especially as primary minerals (e.g. cobaltite, CoAsS, Fleet and Burns 1990; and skutterudite, CoAs₃, Schumer *et al.* 2017) in cobalt sulfarsenide deposits (Leblanc and Billaud 1982) and in secondary sulfates and arsenates (e.g. apowite, CoSO₄·4H₂O, Jambor and Boyle 1965; and erythrite, Co₃(AsO₄)₂·8H₂O, Wildner *et al.* 1996) in the oxidation zone of these deposits (Lorca and Monchoux 1991).

This study investigated soils from Australia, a country that has vast Co reserves, from which only a small amount is currently mined (Geosciences Australia 2023). We collected cobalt-rich soil samples from four different deposit types across arid to semi-arid environments in the Australian interior: lateritic, sulfarsenide-hosted, siderite-hosted and pyrite-hosted (see Table 1). We investigated Co by employing techniques to study its behaviour at the nano-scale, performed analysis on nanoparticles (NPs) in each regolith sample and compared elemental associations and the oxidation state of Co in selected soil samples.

The analysis of NPs is challenged by their elusive nature and the fact that their properties and behaviour are dependent on various characteristics such as number concentrations, mass and size distributions, and composition as well as variable phase and species identity. Single particle inductively coupled plasma–mass spectrometry (SP ICP-MS) has become one of the most powerful methods to count individual NPs and to determine their mass, size and composition alongside determining ionic species. The concept of SP ICP-MS is based on the analysis of diluted NP suspensions and the individual delivery of intact particles into the plasma, where they are entirely atomised. Following an ionisation step, elemental cations are extracted in discrete ion clouds that, following mass filtering and detection, create distinguishable pulses. The number and signal intensity of pulses are respectively proportional to the number concentration and element masses in the particles and can be calibrated by analysing adequate standards in parallel (Mozhayeva and Engelhard 2020; Flores *et al.* 2021). Although common quadrupole-based ICP-MS may only be employed to target a single isotope per particle, a time of flight (ToF)-based mass analyser can overcome this restriction and may additionally interrogate element composition in single particles (Lockwood *et al.* 2024). Our work provides a baseline study for cobalt-based

Table 1. Summary table showing site detail, ordered by deposit type (sulfide, carbonate, oxide-hosted).

| Site name | Sample codes | Coordinates | Climate (Köppen code) | Sampling locality description | Mineralogy | Number of sites for SP ICP-MS analysis |
|-------------------------------|----------------|-------------------------|-----------------------|---|---|--|
| Queen Sally prospect, Qld | QS1 to QS4 | 20.08230°S, 140.15291°E | BSh (Hot semi-arid) | Small Co sulfarsenide prospect | Cobaltite, heavily weathered to arsenates | 4 |
| Mount Cobalt IOCG, Qld | MC1 to MC7 | 21.73709°S, 140.49278°E | BSh | Co sulfarsenide IOCG deposit, formerly mined | Cobaltite, heavily weathered to arsenates | 7 |
| Pyrite Hill, Broken Hill, NSW | PH111 to PH117 | 32.09239°S, 141.19458°E | BWh (Hot Desert) | Pyrite hosted deposit, surface highly weathered | Co-bearing pyrite, heavily weathered with Fe oxide crusts | 6 |
| Young's Cobalt prospect, SA | YCPI to YCP3 | 31.11972°S, 138.67583°E | BSh | Siderite hosted prospect, most outcrop removed | Siderite with quartz | 3 |
| Copperado, Redbank, NT | Copp1 to Copp5 | 17.06271°S, 137.81678°E | BSh | Lateritic Mn-rich outcrop, 100-m diameter | Manganese oxides, Co-, Ni- and Cu-bearing | 5 |
| Calvert, Redbank, NT | Calv1 to Calv3 | 17.19348°S, 137.48986°E | BSh | Small lateritic outcrop of Mn-rich boulders | Manganese oxides, Co-, Ni- and Cu-bearing | 3 |

SP ICP-MS, single particle inductively coupled plasma–mass spectrometry.

NPs in the regolith, showing for the first time that nanoparticulate Co is common in Co-enriched surface environments and forms an important part of its biogeochemical cycling.

Experimental

Sample collection

We collected samples from six localities comprising four separate deposit types in a July 2022 field campaign (see Fig. 1 and Table 1 for sample locations and an image of each site). During sampling, the weather was dry and sunny (daytime maxima 20–27°C) at the northern sampling sites (NT and Qld), and dry but cooler and partly cloudy (daytime

maxima 15–20°C) at the southern sampling sites (SA and NSW). The localities are:

- Two weathering cobalt sulfarsenide deposits near Cloncurry, Queensland, 150 km apart from each other but with similar mineralogy (Queen Sally, abbreviated to QS, and Mount Cobalt, MC)
- A pyrite-hosted deposit 25 km west of Broken Hill, New South Wales (Pyrite Hill, PHill)
- A siderite-hosted outcrop in the Flinders Ranges near Blinman, South Australia (Young's Cobalt prospect, YCP)
- Two lateritic Mn–Co oxide outcrops in the Calvert area of the Northern Territory, 50 km apart from each other (Copperado, Copp and Calvert, Calv)

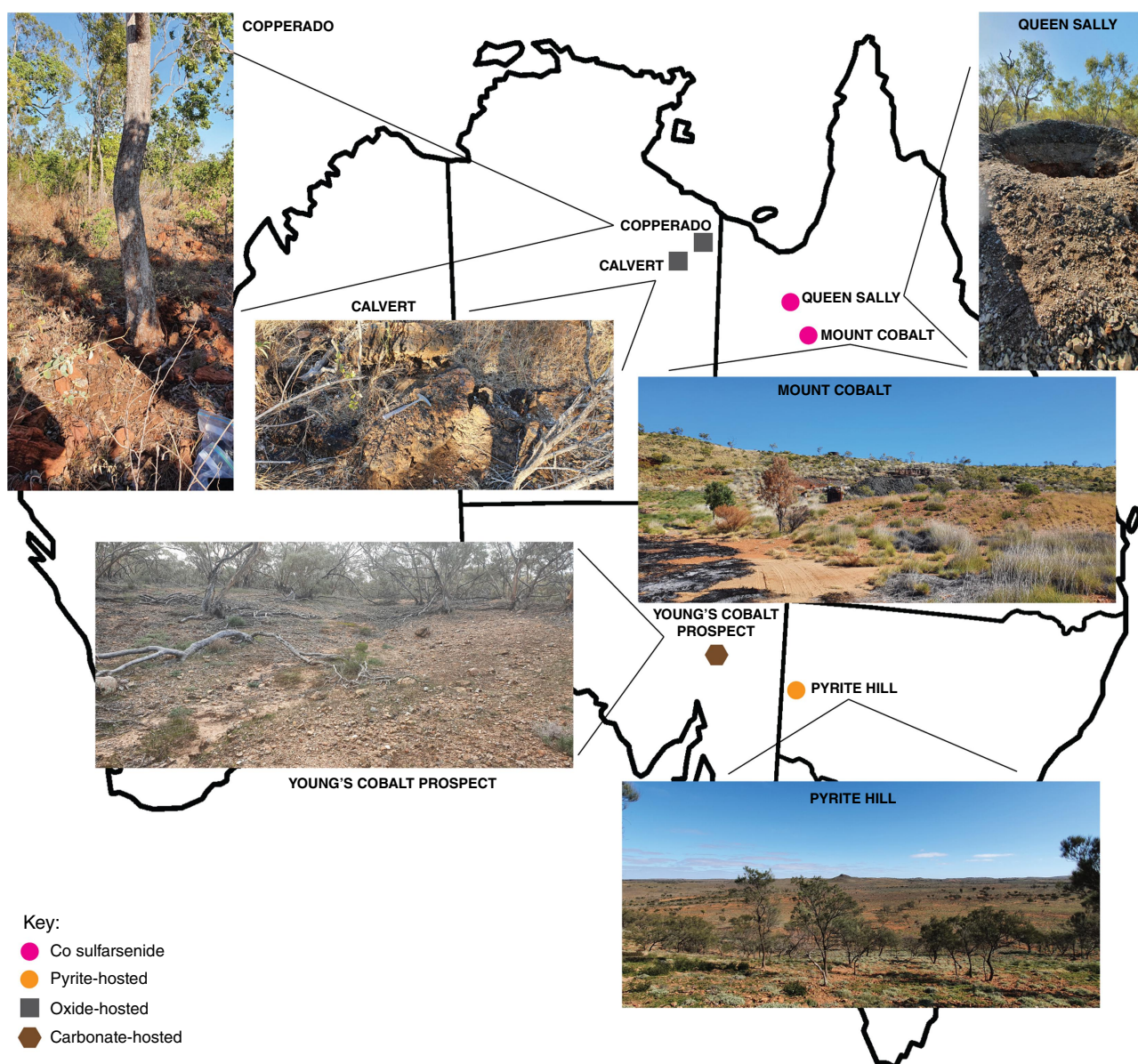


Fig. 1. Map of sampling locations including images of the arid to semi-arid landscapes.

No sites had any nearby water (neither lakes nor permanent streams) at the time of sampling. Samples were collected using sterile equipment under aseptic conditions, using nitrile gloves at all times. Sieves and trowels were rinsed with methylated spirits between each sampling site, and soils were collected from a depth of 10–20 cm, sieved through a 2-mm plastic mesh and collected into pre-sterilised vials. Full descriptions of the development of these sampling methods are provided in Fairbrother *et al.* (2013) and Reith *et al.* (2010, 2012).

Extraction of Co- and Mn-based nanoparticles from soil

For SP ICP-MS analysis, NPs were extracted from soils and suspended in an aqueous phase. A protocol for NP extractions was adopted from Gao *et al.* (2020). Briefly, 0.5 g of soil sample were accurately weighed, placed in a 50-mL polypropylene centrifuge tube and mixed with 50 mL of 2.5-mM tetrasodium pyrophosphate (TSPP, prepared in ultra-pure water with a final pH of 9.6). After shaking in a constant temperature water bath for 30 min (25°C) and following 30 min of sonication, samples were settled at room temperature for 16–18 h in the dark, allowing larger soil particles to precipitate. Supernatants containing extracted NPs were subsequently filtered through 0.45- μm syringe filters (Nylon Filter, Watman, GE Healthcare Life Sciences, UK) and diluted 1:100 with ultrapure water prior to SP ICP-MS analysis.

Single particle inductively coupled plasma–mass spectrometry (SP ICP-MS)

SP ICP-MS was used to quantitatively detect single Co-based and Mn-based NPs in the soil sample extracts and to study their characteristics on a single particle basis. An 8900 series ICP-MS system (Agilent Technologies, Santa Clara, CA, USA) was equipped with platinum cones and x-lenses, and operated with MassHunter software (Agilent Technologies) in ‘single particle’ mode (quadrupole dwell time 0.1 ms). A Scott-type double-pass spray chamber (Glass Expansion, Melbourne, Vic., Australia) was cooled to 2°C and a MicroMist concentric nebuliser (Elemental Scientific, Omaha, NE, USA) was used for sample nebulisation. For the analysis and calibration of SP data sets, a previously developed open-source Python-based data processing platform ‘SPCal’ (ver. 1.1.2, see <https://github.com/djdt/spcal/releases/tag/v1.1.2>) was used (Lockwood *et al.* 2021). Size values were calculated assuming particles are spherical with an average spinel-like formula (CoMn_2O_4 , density 5.09 g cm⁻³; Habjanič *et al.* 2014). Ionic response factors were calculated based on a 10 ng g⁻¹ ICP-MS standard. Transport efficiencies were calculated by the ‘size method’ (Lockwood *et al.* 2021) analysing 100-nm-sized Au NPs (nanoComposix, San Diego, CA, USA, in 0.2-mM citrate). SP ICP-MS results are reported by

site in Table 2, with full results in Supplementary Table S1. Representative size distributions are shown in Fig. 2.

SP ICP-ToF-MS

To investigate the Co:Mn composition of individual particles, SP ICP-ToF-MS was used. A Vitesse ICP-ToF-MS system from Nu instruments (Wrexham, UK, see <https://www.nu-ins.com/products/hr-mc-icp-ms/vitesse>) was employed in single particle mode recording mass spectra from 42 to 250 amu at 12.85 kHz (corresponding to a spectra saving interval of $\sim 80 \mu\text{s}$). Data were recorded using NU CODAQ VITESSE software (ver. 1.5.8267.1) and processed by a modified version of SPCal (ver. 1.1.2) from Lockwood *et al.* (2021). The ICP-ToF-MS instrument was equipped with a concentric nebuliser and its transport efficiency was determined to be 0.8%, obtained by analysing a diluted 100-nm Au NP standard from nanoComposix (San Diego, CA, USA, in 2-mM citrate buffer) and a 10 ng g⁻¹ ionic standard while determining the uptake flow rate. To distinguish background and noise from SP signals, Compound Poisson statistics ($\alpha = 10^{-6}$) were applied while using a log-normal approximation method as discussed in a recent study (Gonzalez de Vega *et al.* 2023). Elements with at least 200 data points per million data points above the particle decision limit were selected for a correlative analysis of coinciding signals and for further calibrations. Here, contiguous signal regions above the signal mean with at least one point above the decision limit were accumulated and calibrated using respective ionic standards diluted to 10 ng g⁻¹. To isolate particle events associated with Co and Mn, a compositional filter was used to limit the analysis solely to Co- and Mn-containing particles. Following calibration, molar ratios of single particles were evaluated in a scatter plot. A linear fit was used and reported as an average Co:Mn molar ratio. Data not containing values for Co:Mn ratios did not contain both Co and Mn with masses over the mass detection limits, which ranged between 20 and 80 ag depending on the ionic background values of sample extracts. Particle compositions were determined using hierarchical agglomerative clustering of normalised elemental mass fraction, with a Euclidean distance cutoff of 20% (Tharaud *et al.* 2022). This rather large distance threshold was chosen to determine the overall mean Co:Mn molar ratios in single particles rather than cluster numbers and their individual composition.

Synchrotron X-ray analyses

Regolith samples were prepared for analysis by double impregnation in epoxy resin, following the method described in Missen *et al.* (2022a) and briefly re-described here. These Co-rich regolith samples are deposited in the Museums Victoria Petrology collection (sample number E20470). First, ~ 0.5 g of resin was added to a 0.7-mL vial (top diameter ~ 7 mm) of the sample and allowed to cure.

Table 2. Summary table showing averaged data relating to both Co- and Mn-containing NPs.

| Site name | Number of Co NPs ($n \text{ g}^{-1}$ regolith) | Mean Co-based NPs size (nm) | Mass of Co NPs (ng g^{-1} regolith) | Average regolith Co (ppm) | Co NPs/total Co (%) | Number of Mn NPs ($n \text{ g}^{-1}$ regolith) | Mean Mn-based NPs size (nm) | Weight of Mn NPs (ng g^{-1} regolith) | Average regolith Mn | Mn NPs/total Mn (%) | Mean molar ratio of Co:Mn in ToF data (sample size) |
|-----------------------------|---|-----------------------------|---|---------------------------|---------------------|---|-----------------------------|---|---------------------|---------------------|---|
| Queen Sally Prospect, Qld | $(2.19 \pm 0.04) \times 10^8$ | 111 | 990 | $>6.6 \times 10^3$ | <0.016 | $(6.7 \pm 0.4) \times 10^7$ | 35 | 9.5 | 730 ppm | 0.0014 | 0.70 (4) |
| Mount Cobalt, Qld | $(2.40 \pm 0.04) \times 10^8$ | 71 | 229 | 880 | 0.034 | $(6.6 \pm 0.4) \times 10^7$ | 37 | 10.8 | 357 ppm | 0.0032 | 0.69 (4) |
| Pyrite Hill, NSW | $(6.0 \pm 0.2) \times 10^7$ | 36 | 10.2 | 40 | 0.025 | $(4.5 \pm 0.3) \times 10^7$ | 41 | 10.9 | 232 ppm | 0.0045 | 0.22 (2) |
| Young's Cobalt prospect, SA | $(1.10 \pm 0.09) \times 10^7$ | 36 | 5.1 | 6.8 | 0.064 | $(1.02 \pm 0.04) \times 10^8$ | 36 | 14.8 | 326 ppm | 0.0049 | 0.30 (1) |
| Copperado, NT | $(1.28 \pm 0.03) \times 10^8$ | 37 | 36.1 | 115 | 0.075 | $(8.1 \pm 0.4) \times 10^7$ | 55 | 49.5 | 0.160% | 0.0053 | 0.10 (1) |
| Calvert, NT | $(1.20 \pm 0.03) \times 10^8$ | 31 | 10.8 | 178 | 0.007 | $(1.62 \pm 0.05) \times 10^8$ | 92 | 358 | 2.06% | 0.0022 | 0.10 (1) |

Throughout the table, regolith refers to the sub 2-mm fraction of surface samples collected in this study. Samples were crushed before bulk chemical analysis, but not for SP ICP-MS.

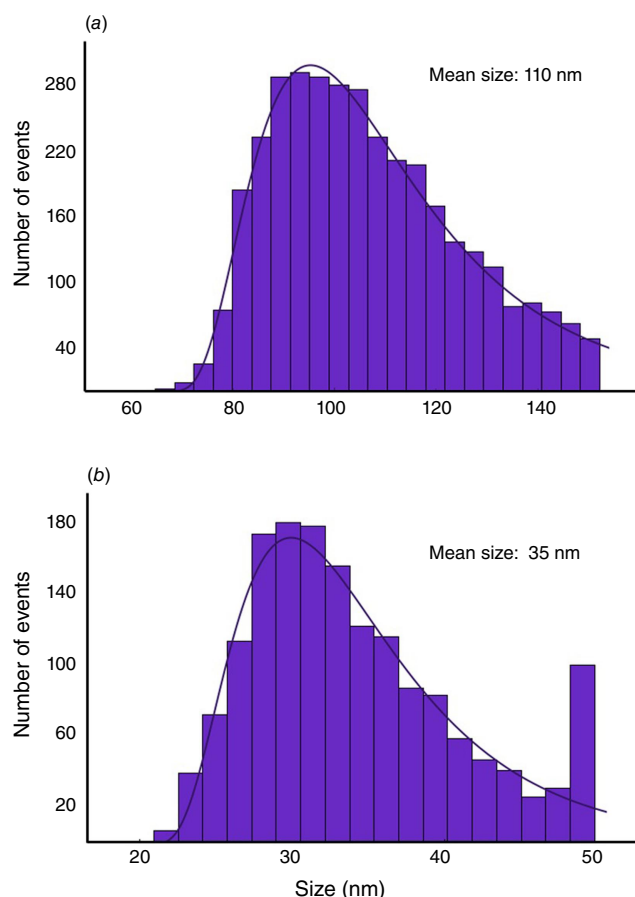


Fig. 2. Size distributions of Co-based NPs for samples (a) Queen Sally sample Q51 and (b) Copperado sample Copp5. Sizes were estimated using mass fractions and densities of CoMn_2O_4 .

Subsequently, groups of six vials were placed upside down in a 2.5-cm mould and ~ 3.0 g of resin was again added to encase these six vials into a 2.5-cm diameter puck. A small rotary saw was used to cut the pucks to a height of ~ 0.6 cm, then polishing and grinding of the puck to a surface fineness of $1\ \mu\text{m}$ was performed using oil-based lubricants to ensure that no clays or water-soluble phases dissolved during the polishing. The synchrotron analyses were undertaken at the ID21 beamline of the European Synchrotron Radiation Facility (ESRF), France with data preserved online (Missen *et al.* 2022b). Data were collected at the Co *K*-edge (7709 eV).

XFM (X-ray fluorescence microscopy) and XANES (X-ray absorption near-edge spectroscopy) measurements were performed using the scanning X-ray microscope at beamline ID21, ESRF. XFM mapping was performed at 7900 eV with a dwell time of 0.1 s using a $0.3\text{-}\mu\text{m}$ vertical $\times 0.7\text{-}\mu\text{m}$ horizontal Kirkpatrick–Baez focused beam with an average flux of 1.2×10^{10} photons s^{-1} , the energy selection was carried out by means of a Si (111) double crystal monochromator. XRF (X-ray fluorescence) emission spectra were obtained with a silicon drift detector (SDD) of area $80\ \text{mm}^2$ of active area (SGX SensorTech, RaySpec Ltd, UK). The XRF maps

(Fig. 3) were processed using an open source code (see https://gitlab.com/EduardoV/xas_tools) combined with PyMCA software (ver. 5.9.2, see <https://www.silx.org/doc/PyMca/dev/index.html>; Solé *et al.* 2007) to fit the element emission lines, correct detector dead time and normalisation by incoming beam intensity. From the Co distribution in the sample, points of interest were selected for Co *K*-edge XANES scans using a 7709-eV reference energy in fluorescence yield (FY), beginning 10 eV before and finishing 140 eV after the reference energy. A step size of 0.5 eV and a dwell time of 0.1 s was used for collecting XANES scans, and scans were generally completed in triplicate. XRF and X-ray absorption spectroscopy (XAS) measurements were performed at the ESRF, France (Proposal number EV-506; Missen *et al.* 2022b).

The following materials were utilised for calibration of the beamline and for comparison with analytical samples: Co metal foil (Co^0), cobalt(II) oxide ($\text{Co}^{\text{II}}\text{O}$), cobalt(II,III) oxide (Co_3O_4 i.e. $\text{Co}^{\text{II}}\text{Co}^{\text{III}}_2\text{O}_4$), a sample labelled heterogenite (Museums Victoria Mineralogy collection, sample number M42912), which further analysis showed contained some Co^{II} as well as Co^{III} , and Co^{III} -bearing Mn oxide from Copperado. Principal component analysis (PCA) was applied on all μXANES data, performed with Orange software (ver. 3.36.2, see <https://orangedatamining.com/>; Demšar *et al.* 2013), including the add-on ‘Spectroscopy’ (Toplak *et al.* 2017). PCA was implemented on the second derivative of the spectra (using the Savitzky–Golay method, second polynomial order and 15 points window) and a vector normalisation. The spectra from clusters observed in the PCA plots were grouped using the *k*-means method and subsequently normalised following the XAS normalisation widget in Orange software (Spectroscopy add-on).

Bulk regolith analysis

Determination of bulk Co and Mn contents in the regolith was performed by ALS Geochemistry. Samples (previously sieved through a 2-mm plastic mesh as described above) were pulverised until 85% of the sample passed through a $75\text{-}\mu\text{m}$ filter, then analysed by a method employing an aqua regia digestion followed by ICP-MS analysis (ALS code ME-MS41L). Co and Mn results for each site are reported in Table 2 and were used to determine the ratio of nanoparticulate Co and Mn to Co and Mn in the $<2\text{-mm}$ regolith fraction, with full results by sampling location in Supplementary Table S1.

Results

Cobalt- and manganese-based nanoparticles

Both Co- and Mn-containing NPs were extracted and detected in all 28 soil samples using SP ICP-MS, with a summary of results shown in Table 2. Two different SP ICP-MS methods were used. First, a quadrupole-based SP

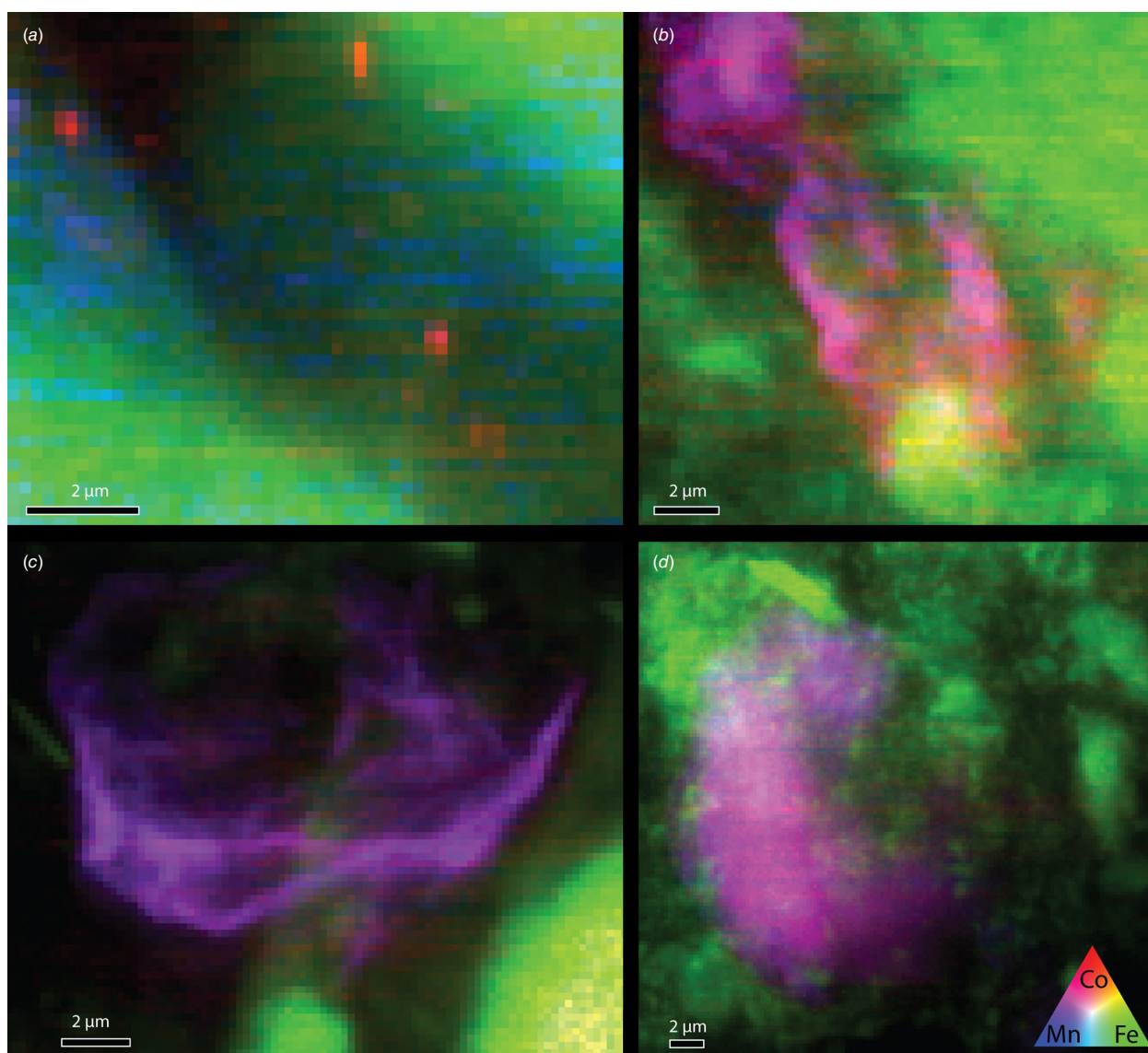


Fig. 3. XFM maps presented in RGB (red–green–blue) format showing distribution of Co (red) relative to iron (green) and Mn (blue). The characteristic association of Co and Mn is shown by the purple overlap colour of red (Co) and blue (Mn). Pixel size for the maps is $200 \times 200 \text{ nm}^2$. (a) Queen Sally (subsample QS1), one of the few samples with cobalt oxide NPs separate from Mn. (b) Mount Cobalt (subsample MC4). (c) Pyrite Hill (subsample PHill2). (d) Copperado (subsample Copp4).

ICP-MS set-up was employed, which is characterised by its high detection power and therefore its ability to detect even small Co or Mn particulate masses. However, a disadvantage of quadrupole-based SP ICP-MS is that Co and Mn could not be analysed simultaneously. Therefore, SP ICP-ToF-MS was used in a subsequent step enabling the simultaneous acquisition of almost all element signals in a single particle. Despite lower detection power, this enabled the determination of compositions on a single particle level. As a focus of this study, molar ratios between and Co and Mn were determined, and values are listed in Table 2 (ratios for each sampling site are in Supplementary Table S1). However, in a non-target approach, other elements associated with Co

were investigated qualitatively. Samples without reported mass composition either had no particles containing both Mn and Co, or particles were too small to be detected in SP ICP-ToF-MS, which had approximately one order of magnitude higher mass detection limits compared to quadrupole-based SP ICP-MS (size detection limit, sDL, for Mn and Co were 31.6 and 27.7 nm respectively). Owing to the characteristics of quadrupole and ToF-based SP ICP-MS, the former was used to determine mass and size distributions, whereas the latter was employed for compositional analyses. In the present study, we found evidence that a majority of Co and Mn is present in a CoMn_2O_4 phase, which was therefore selected as proxy to estimate size distributions. However,

particulate mass distributions of elements can be determined without knowledge of phases allowing a less biased view (Table 2). The three highest concentrations of extractable Co-based NPs were found in three of the four weathering sulfarsenide Queen Sally samples (1262 ± 21 , 1390 ± 41 and 1236 ± 30 ng NP Co g⁻¹ regolith, subsequently written as nanograms of Co per gram for simplicity), with an average number of $2.19 \pm 0.04 \times 10^8$ NPs g⁻¹. Only sample QS4 had a lower concentration (71 ± 1 ng Co g⁻¹), which was likely due to sampling further from the deposit rather than from the actively weathering zone. The two samples with the lowest average number of Co NPs were found in sampling sites at siderite-hosted Young's Cobalt prospect (0.69 ± 0.08 and 0.94 ± 0.18 ng Co g⁻¹, average number of NPs $(1.10 \pm 0.09) \times 10^7$ NPs g⁻¹). Other samples with high average concentrations of Co-containing NPs included those from the other weathering sulfarsenide deposit Mount Cobalt (average 229 ± 7 ng Co g⁻¹ from $(2.40 \pm 0.04) \times 10^8$ NPs g⁻¹, $n = 7$, varying between 30 ± 1 and 867 ± 25 ng Co g⁻¹) and lateritic Copperado (average 36 ± 1 ng Co g⁻¹ from $(1.28 \pm 0.03) \times 10^8$ NPs g⁻¹ with $n = 5$, dominated by 129 ± 3 ng Co g⁻¹ in sample Copp4, with an average of 12.9 ± 0.4 ng Co g⁻¹ in the other four samples). Size distributions of the Co-based NPs typically showed an average size of 55 ± 38 nm, with significant variation in mean sizes with 110 nm for QS1 and 35 nm for Copp5 (Fig. 2).

Owing to the prevalent association of Co with Mn (see *Synchrotron: NP agglomerates, Co oxidation state and elemental associations* below), we also analysed the concentration of Mn-based NPs in the regolith samples using SP ICP-MS. The concentration of Mn-based NPs was highest at the Calvert lateritic Mn–Co oxide prospect, averaging 358 ± 14 ng NP Mn g⁻¹ regolith, subsequently written as nanograms of Mn per gram (highest value 486 ± 24 ng Mn g⁻¹ at sample Calv1) from an average of $(1.62 \pm 0.05) \times 10^8$ NPs g⁻¹. The other Mn–Co prospect Copperado had the next highest nanoparticulate Mn contents averaging 49 ± 2 ng Mn g⁻¹ from $(8.1 \pm 0.4) \times 10^7$ NPs g⁻¹. Sample Copp4 had the highest NP Mn content (111 ± 6 ng Mn g⁻¹) of the 5 Copperado sites as well as having the highest NP Co content. Across the other four sites, the average concentrations of Mn-based NPs were consistently between 9 and 15 ng Mn g⁻¹, with 9.5 ± 0.5 ng Mn g⁻¹ at Queen Sally, 10.8 ± 0.6 ng Mn g⁻¹ at Mount Cobalt, 14.8 ± 0.7 ng Mn g⁻¹ at Young's Cobalt prospect and 10.9 ± 0.7 ng Mn g⁻¹ at Pyrite Hill. The minimum value across these sites is 4.3 ± 0.3 ng Mn g⁻¹ at sample MC3 and maximum value was 30 ± 1 ng Mn g⁻¹ at nearby site MC5.

Using SP ICP-ToF-MS enabled the study of particle compositions. Besides the calibration of the Co:Mn molar ratio, other elements associated with Co on a single particle basis were investigated. Fig. 4a, b shows the transient raw data of SP ICP-ToF-MS and demonstrates the coincidental detection of Co (yellow) with different elements including Ti (blue),

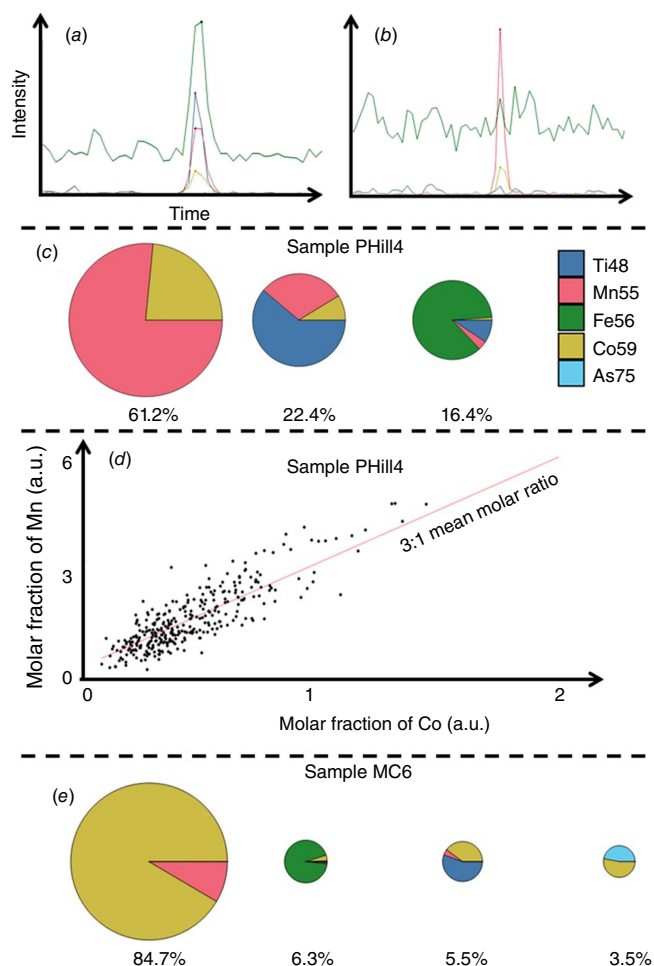


Fig. 4. (a, b) Transient raw data of SP ICP-ToF-MS. (c) Molar composition of three groups of Co-containing NPs found in sample PHill4 as representative sample. (d) Distribution of Mn and Co in the 61.2% of Pyrite Hill sample PHill4 Mn–Co oxide NPs at an approximate ratio of 3:1 Mn:Co. (e) Representative Mount Cobalt sample MC6, for which significantly more Co relative to Mn was contained in individual NPs.

Mn (red), Fe (green) and As (cyan) on a single particle level. Fig. 4c shows the composition of Co-containing NPs found in sample PHill4 as a representative sample (weathering pyrite environment). It is evident that three different groups were identified. The largest fraction (61.2%) contained Mn and Co at an approximate ratio of 3:1 as plotted in Fig. 4d. It was determined that 22.4% of the NPs contained Ti as well as Co and Mn (approximate Ti:Co:Mn ratio 5:2:1) and 16.4% contained mainly Ti and Fe (with minor Co and Mn) in individual particles. The compositional analysis of Co-NPs found that most particles were associated with Mn. However, the relative fraction of Mn to Co varied across different sampling locations. Fig. 4e shows representative sample MC6 (weathering sulfarsenide), for which the highest molar fraction of Co relative to Mn was contained in individual particles (84.7%). Furthermore, respectively 6.3

and 5.5% additionally contained Fe or Ti, and 3.5% of particles consisted of As and Co.

Synchrotron: NP agglomerates, Co oxidation state and elemental associations

Agglomerates (in the physical, not statistical sense) of Co-based NPs were at the most 20 μm in cross-sectional breadth, but were generally $<1\ \mu\text{m}$ in size (Fig. 3). Using XANES, the most prevalent Co oxidation state across all samples was a mixture of +II and +III (Fig. 5 and 6), although the +III oxidation state was generally more dominant. Several samples showed distinct clusters of spectra in PCA figures (Fig. 5; clusters determined mathematically by the *k*-means method) when plotting the variation of sample

spectra to the analytical standards. Detailed analysis of our synthetic and natural compounds led to the following choices for the standards used as references for the *k*-means method: cobalt(II) oxide for Co^{II} , the heterogenite sample for mixed $\text{Co}^{\text{II}}/\text{Co}^{\text{III}}$ and a rock crust of Co^{III} -bearing Mn oxide from Copperado for Co^{III} . Heterogenite and lithium cobalt(III) oxide ($\text{LiCo}^{\text{III}}\text{O}_2$) were intended as the initial standards for Co^{III} but were shown to contain minor traces of Co^{II} based on their XANES spectra, thus the most oxidised sample we analysed (Co^{III} -bearing Mn oxide from Copperado) was chosen as the Co^{III} standard. The case of heterogenite may be that the heterogenite sample contains minor Co^{II} with a potential formula of $\text{HCo}^{\text{II}}_x\text{Co}^{\text{III}}_{1-x}\text{O}_{2-x+2}$ (x likely <0.2) or more likely that a Co^{II} bearing mineral such as goite ($\text{Co}^{\text{II}}\text{Co}^{\text{III}}_3\text{O}_4$; Lei *et al.* 2022) was

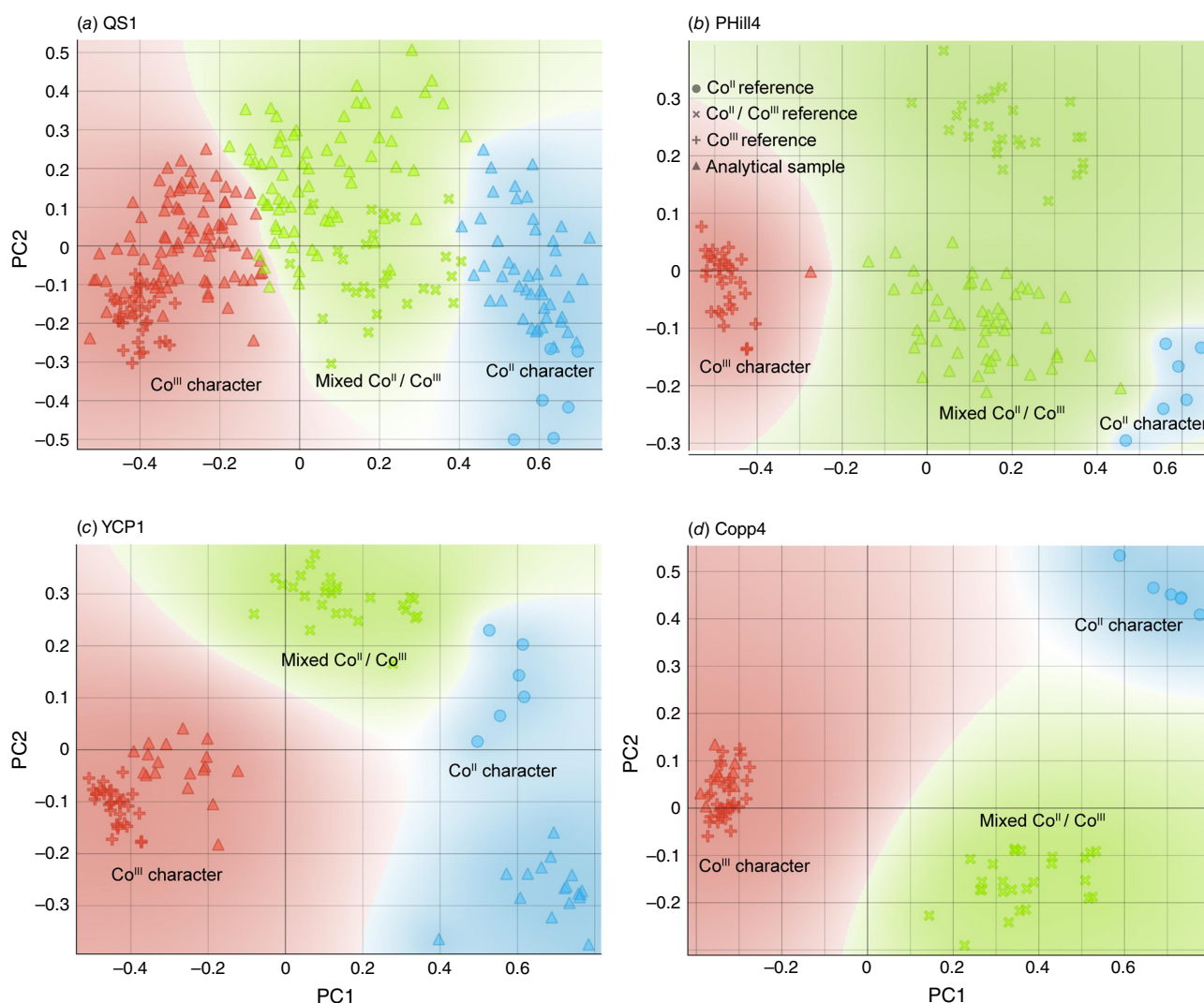


Fig. 5. PCA comparisons for sampling sites using the *k*-means method to select three groups (Co^{II} , $\text{Co}^{\text{II}}\text{--}\text{Co}^{\text{III}}$ and Co^{III} character) showing (a) Queen Sally sample QS1, (b) Pyrite Hill sample PHill4, (c) Young's Cobalt prospect sample YCP1 and (d) Copperado sample Copp4 as representative samples. Standards included to generate the PCA figures are $\text{Co}^{\text{II}}\text{O}$ (right hand side of PCA figures, circles), natural heterogenite (central area, cross symbols), Co^{III} -bearing Mn oxide (left hand side, plus symbols) and finally the sample itself (triangles) in the PCA maps for comparison.

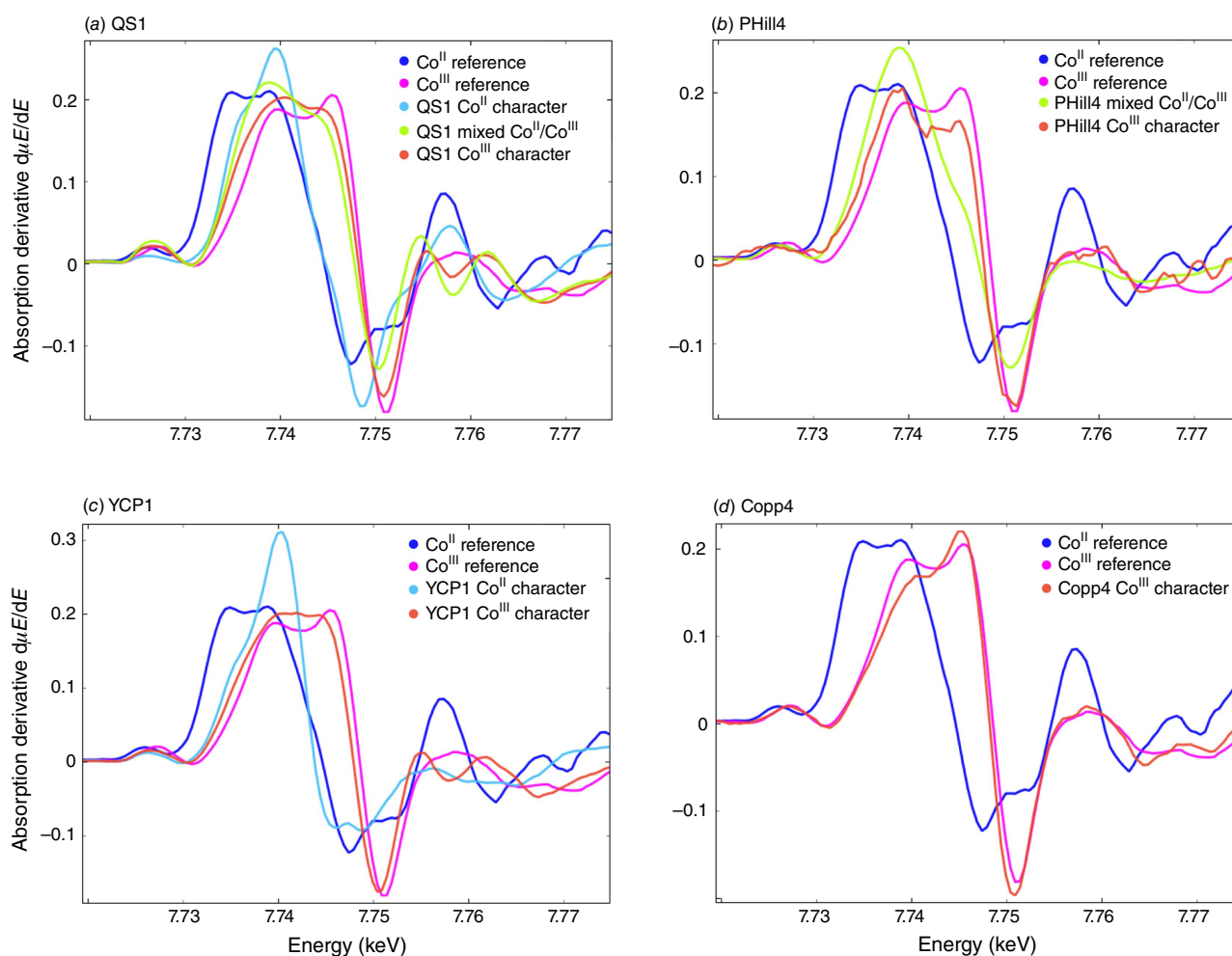


Fig. 6. First derivative of XANES spectra (grouped in PCA using Orange software then averaged) for the samples (a) Queen Sally sample QS1, (b) Pyrite Hill sample PHill4, (c) Young's Cobalt prospect sample YCP1 and (d) Copperado sample Copp4.

intermingled with an especially heterogeneous heterogenite sample.

Clustering showed that samples may contain groups of Co NPs with 1, 2 or 3 clusters of oxidation states represented (Fig. 6). Localities such as PHill4 (all mixed oxidation state, Fig. 5b, 6b) and Copp4 (all Co^{III}, Fig. 5d, 6d) contained Co-based NPs with just a single oxidation state group represented. Young's Cobalt prospect sample YCP1 contained distinct clusters of Co^{II} and Co^{III}-based NPs but no mixed oxidation state NPs (Fig. 5c, 6c). Other sampling localities (e.g. QS1 and MC1 from weathering sulfarsenide localities; QS1 shown in Fig. 5a, 6a) showed the presence of all of Co^{II}, Co^{III} and mixtures of the two oxidation states in the regolith. These observations suggest that Co-based NPs form with different mineral identities (e.g. heterogenite NPs with mainly Co^{III}, spinel-based NPs with both Co^{II} and Co^{III}, Co^{II} arsenates or oxides with Co^{II}).

XFM results showed that the major association of Co in the regolith samples was not with Fe, despite its prevalence in all samples. Instead, in most analysed localities, Co and

Mn were observed in close association, with the Co and Mn signal in the XRF maps typically overlapping in all samples except some parts of the Co-rich Queensland sulfarsenide localities. No association with S was observed in these supergene samples. This observation led to the hypothesis, subsequently verified by SP ICP-ToF-MS, that the NPs detected by SP ICP-MS are not formed of individual Co- (or Mn-) oxide NPs but comprise both Co and Mn in Co-Mn oxide NPs.

Discussion

Cobalt cycling in terrestrial environments

In Fig. 7, we present a diagram of cobalt cycling in surface environments with a focus on Co(-Mn) nanoparticulate phases. Co cycling in surface environments begins with dissolution of solid Co-bearing phases to form soluble Co^{II} (Fig. 7, Process 1). Sulfides and sulfarsenides are typical

primary hosts of cobalt (including examples with both cobalt as a trace element and as a mineral-defining species) along with Co hosted by primary oxides and carbonates (Co within lateritic deposits may be considered as forming later in this cycle). After dissolution, several processes can take place. Formation of secondary oxysalt minerals (Fig. 7, Process 2) may be followed by redissolution back to Co^{II} (Fig. 7, Process 6), however formation of Co^{III} oxide minerals is less likely to be followed by redissolution due to the higher stability of these phases – for instance, heterogenite does not dissolve unless the Co^{III} is reduced back to Co^{II} (Dehaine *et al.* 2021).

The most important insight obtained by SP ICP-MS and synchrotron XFM was the formation of Co(–Mn) oxide NPs (Fig. 7, Process 5). These Co-containing NPs may form from physical weathering of Co-bearing Fe- or Mn-oxides (Fig. 7, Process 7) or may be mediated by a microbial process. Co(–Mn) oxide NPs may re-dissolve in the presence of rain, surface and ground waters, but the main two processes expected to be key to NP mobility are sorption (Fig. 7, Process 8) to either organoclays or to Fe-, Mn- or Co-oxide minerals. Redox drivers for the dynamic Fe (Kappler *et al.* 2021) and Mn (Li *et al.* 2021) cycles are likely to govern Co mobility due to their general predominance over Co in most surface environments, although the availability and behaviour of Co oxidation states is different to that of Mn and Fe. Desorption (Fig. 7, Process 9) may release the Co(–Mn) oxide NPs back to being free NPs, whereas plant-based uptake of Co (Fig. 7, Process 3) may occur directly from soluble Co^{II} in pore water and from Co(–Mn) oxide NPs (either free or sorbed on organoclays). From plants, Co can be incorporated into other biota where a range of interactions may take place. Although these interactions

are beyond the scope of this paper, they are likely important for the cycling of Co through living organisms and back into the environment (e.g. decomposition of plants enriched in Co would result in Co being returned to the environment: Fig. 7, Process 10).

The extent to which microbes are involved in mediating cobalt cycling processes is not yet known. Iravani and Varma (2020) showed that differing conditions for Co-(hydr)oxide NP formation leads to different crystallinity and morphology of the products, processes that are complicated further in the natural environment by the presence of other elements such as Fe and Mn. *Microbacterium* sp. MRS-1 has been shown to produce Co_3O_4 from soluble Co^{II} cations (i.e. laboratory evidence for Fig. 7, Process 5) (Sundararaju *et al.* 2020). Although Co-oxide based NPs are likely less toxic to most microbes than soluble Co^{II} , several studies have also determined their high toxicity when present as Co_3O_4 . These results indicate the potential toxicity of produced NPs and their capacity to alter a local biome by their toxicity towards non-Co-resistant species including microbes (Khan *et al.* 2015; Moradpoor *et al.* 2019) and plants (Ghodake *et al.* 2011) (see Fig. 7, Processes 3 and 11).

In the warm to hot Australian arid and semi-arid environments where the sampling campaign was conducted, yearly rainfall is low, and soils typically have low moisture content. The degree to which Co is cycled in Co-rich environments varies, with dissolution rates (especially of ephemeral phases, compared to releasing Co from Co-rich Fe–Mn oxides) at a maximum following rainfall. In this regard, the Fe–Mn oxide-hosted cobalt prospects of Copperado and Calvert are different to their southern counterparts, with a clear distinction between dry and wet seasons despite the overall semi-arid conditions.

Cobalt oxide nanoparticle regolith cycling schematic

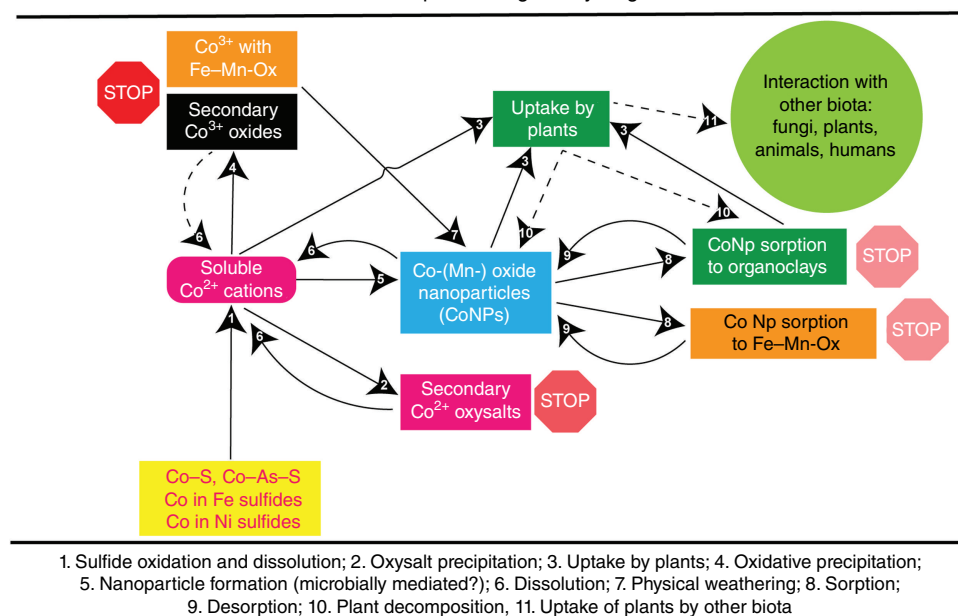


Fig. 7. Schematic of cobalt-based nanoparticles in the environment.

Association of Co with Mn and other elements

In most of our analysed samples, Co was found associated with Mn through both SP ICP-ToF-MS and XRF. The latter revealed groups of NPs varying in size from $<1\ \mu\text{m}$ to up to $20\ \mu\text{m}$ (Fig. 3). The only larger sizes (up to $100\ \mu\text{m}$) of Co-enriched regolith zones were identified in highly Co-enriched samples from Mount Cobalt and Queen Sally (880- and >6600 -ppm Co average concentrations at these two sites respectively). The chemical form of the Co-containing NPs is likely to be a Co–Mn oxide. The pure end-members of the Co and Mn oxyspinel family are respectively goethite, Co_3O_4 (Lei *et al.* 2022), and hausmannite, Mn_3O_4 (Baron *et al.* 1998). Potential intermediates CoMn_2O_4 (Habjanič *et al.* 2014) and MnCo_2O_4 (Das Sharma *et al.* 2011), possible species of the Mn–Co oxide phases observed by XRF in this study, have not been described as minerals. The SP ICP-ToF-MS data show that Mn is generally the dominant element in the Co–Mn oxide NPs, with an example average 1:3 Co:Mn molar ratio at sampling site Phill4 shown in Fig. 4d. Particles with Co $>$ Mn were observed at two sampling sites in weathering sulfarsenide localities (Co:Mn molar ratio of 1.79 at QS2 and MC1; Supplementary Table S1). However, for the samples in which ToF-MS was able to determine a Co:Mn molar ratio (13 samples), the ratio is <1 in 11 out of 13 samples being between 0.1 and 0.5 in nine of the samples, including all five non-sulfarsenide samples for which a ratio was calculable. Thus, the formula for most of the non-sulfarsenide Co–Mn NPs may be approximated as $(\text{Co}_x\text{Mn}_{1-x})\text{Mn}_2\text{O}_4$ if a spinel model is used. The association of Co with Mn has been observed in lateritic environments, as Mn^{III} and Mn^{IV} are able to oxidise Co^{II} into less mobile Co^{III} (either by inorganic or biologically mediated processes), allowing for structural incorporation into Mn oxides (Tanaka *et al.* 2013; Simanova and Peña 2015; Newsome *et al.* 2020).

Arsenic is often a concern when discussing the environmental impacts of cobalt sulfarsenide mining and ore processing. In the presence of iron oxides and under basic conditions, arsenic is usually stabilised as sorbed complexes on the (oxyhydr)oxides or even as a variety of iron arsenate in minerals such as scorodite (Filippou and Demopoulos 1997; Majzlan *et al.* 2012; Drahota *et al.* 2016). In the weathering environment around the Mount Cobalt and Queen Sally mines, the cobalt and arsenic concentrations are sufficiently high that cobalt arsenate minerals such as erythrite form on the surface of weathering ore (Kloprogge *et al.* 2006; Nagashima *et al.* 2021). In general, arsenic deportment and mobility in tailings has been better studied than that of cobalt, such as at abandoned As–Sb mines in Slovakia (Majzlan *et al.* 2011). However, with the operation of cobalt arsenide mines such as Bou Azzer, Morocco (Ahmed *et al.* 2009; Subías *et al.* 2022), and potential for sites such as Mount Cobalt to reopen to bolster cobalt supplies, understanding the combined behaviour of cobalt and arsenic is important to ensure neither of these elements become environmental contaminants.

Importance of nanoparticles for cycling of Co in surface environments

We detected Co- and Mn-containing NPs in all samples across all analysed sites using SP ICP-MS, encompassing different deposit and climate types as well as widely varying bulk cobalt concentrations, and found that they were associated on a single particle basis. Different mineralogical hosts for cobalt in the outcropping cobalt-rich rocks (Fe–Mn oxides, cobalt sulfarsenides, cobalt-rich pyrite and cobalt-rich carbonates) all contain cobalt-based NPs in surrounding soils. The host rocks provide a source for Co to be released into the environment, and regardless of original lithology (excepting the sulfarsenide sites) XRF maps showed the association of Co and Mn in nanoparticulate regolith phases. High As and comparatively low Mn contents at Queen Sally and Mount Cobalt result in the Co–Mn association not being observed as strongly at these two localities, but it is notable that even at low-Co and carbonate-hosted Young's Cobalt prospect and the pyrite-hosted (i.e. high Fe) Pyrite Hill, the Co–Mn association in weathered regolith samples is strong.

The chemistry and reactivity of the Co-containing NPs is key to the behaviour of the Co stored within them. Unlike reactive elemental or sulfide NPs formed by some elements in the environment, oxide NPs are typically relatively stable (Nair *et al.* 2022). As minerals, the Co^{III} oxyhydroxide mineral heterogenite may persist for almost 1×10^9 years (Decree *et al.* 2014) and oxyspinels such as hausmannite may also be stable for billions of years, for example the hausmannite deposits of Wessels-type ore in the Kalahari manganese field (Vafeas *et al.* 2019). Only more acidic conditions are likely to dissolve Co–Mn oxide phases (e.g. an acid rain event, or the acid-generating dissolution of nearby sulfarsenides or sulfides at relevant sites).

Links to anthropogenic cobalt

The concentrations of Co in natural environments are increasing due to anthropogenic factors, namely the use of metals like Co for new energy storage and generation technologies. Environments that are naturally enriched in Co provide the ideal sites to study Co (bio)geochemical processes, and conclusions drawn on Co cycling in naturally enriched environments are applicable to terrestrial landscapes in which Co is artificially enriched. Our study incorporates both largely undisturbed sites (Copperado, Calvert, Broken Hill) and previously disturbed sites at various stages of remediation (Queen Sally, Mount Cobalt, Young's Cobalt prospect).

Our results suggest that the promotion of more basic conditions to encourage the formation of Mn–Co and Co-dominant (oxyhydr)oxides when processing Co-rich waste materials will result in the best chance of Co being immobilised and not being released to the environment. Acidic

conditions should be avoided when possible to prevent Co, As and other critical or deleterious elements from being dissolved into surface waters. Although Co sulfide and sulfarsenide weathering may release acid, iron sulfides such as Co-bearing pyrite are more likely to be the larger contributors to acid mine drainage environments due to their volume compared to primary Co minerals in most environments. Desulfurisation of sulfides prior to mine waste disposal is likely to prevent mobilisation of Co in tailings dams.

Conclusion

Co is seen as one of the most important commodities of the 21st Century, yet its surface cycling is not well understood compared to its oceanic biogeochemical cycling. We showed that Co-containing nanoparticles are found across arid to semi-arid Co-rich environments in Australia, suggesting the importance of nanoparticulate Co-dominant phases in Co cycling. Both Co- and Mn-containing nanoparticles were detected using SP ICP-MS with average concentrations on the order of 10^7 or 10^8 NPs per gram of regolith. It is worth emphasising that these numbers refer to 'extractable' particles. A maximum of 1390 ± 40 ng NP Co g⁻¹ regolith was detected in the weathering sulfarsenide deposit of Queen Sally. We also highlighted a key association with Mn. This study demonstrates the importance of analysing for nanoparticulate phases in terrestrial environments, even for metal(loid)s that are generally only found as minor or trace elements.

Supplementary material

Supplementary material is available [online](#).

References

- Ahmed AH, Arai S, Ikenne M (2009) Mineralogy and paragenesis of the Co-Ni arsenide ores of Bou Azzer, Anti-Atlas, Morocco. *Economic Geology* **104**, 249–266. doi:10.2113/gsecongeo.104.2.249
- Banza Lubaba Nkulu C, Nawrot TS, Haufroid V, Decrée S, De Putter T, Smolders E, Kabyla BI, Luboya ON, Ilunga AN, Mutombo AM, Nemery B (2009) High human exposure to cobalt and other metals in Katanga, a mining area of the Democratic Republic of Congo. *Environmental Research* **109**, 745–752. doi:10.1016/j.envres.2009.04.012
- Banza Lubaba Nkulu C, Casas L, Haufroid V, De Putter T, Saenen ND, Kayembe-Kitenge T, Musa Obadia P, Kyanika Wa Mukoma D, Lunda Ilunga J-M, Nawrot TS, Luboya Numbi O, Smolders E, Nemery B (2018) Sustainability of artisanal mining of cobalt in DR Congo. *Nature Sustainability* **1**, 495–504. doi:10.1038/s41893-018-0139-4
- Baron V, Gutzmer J, Rundlof H, Tellgren R (1998) The influence of iron substitution in the magnetic properties of hausmannite, Mn²(Fe,Mn)³⁺₂O₄. *American Mineralogist* **83**, 786–793. doi:10.2138/am-1998-7-810
- Calvão F, McDonald CEA, Bolay M (2021) Cobalt mining and the corporate outsourcing of responsibility in the Democratic Republic of Congo. *The Extractive Industries and Society* **8**, 100884. doi:10.1016/j.exis.2021.02.004
- Chandra M, Yu D, Tian Q, Guo X (2022) Recovery of cobalt from secondary resources: a comprehensive review. *Mineral Processing and Extractive Metallurgy Review* **43**, 679–700. doi:10.1080/08827508.2021.1916927
- Chmiel R, Lanning N, Laubach A, Lee J-M, Fitzsimmons J, Hatta M, Jenkins W, Lam P, McIlvin M, Tagliabue A, Saito M (2022) Major processes of the dissolved cobalt cycle in the North and equatorial Pacific Ocean. *Biogeosciences* **19**, 2365–2395. doi:10.5194/bg-19-2365-2022
- Das Sharma A, Mukhopadhyay J, Basu RN (2011) Synthesis and characterization of nanocrystalline MnCo₂O₄-δ spinel for protective coating application in SOFC. *ECS Transactions* **35**, 2509–2517. doi:10.1149/1.3570249
- Decree S, Deloule É, De Putter T, Dewaele S, Mees F, Baele J-M, Marignac C (2014) Dating of U-rich heterogenite: new insights into U deposit genesis and U cycling in the Katanga Copperbelt. *Precambrian Research* **241**, 17–28. doi:10.1016/j.precamres.2013.11.009
- Dehaine Q, Tijsseling LT, Glass HJ, Törmänen T, Butcher AR (2021) Geometallurgy of cobalt ores: a review. *Minerals Engineering* **160**, 106656. doi:10.1016/j.mineng.2020.106656
- Demšar J, Curk T, Erjavec A, Gorup Č, Hočvar T, Milutinovič M, Možina M, Polajnar M, Toplak M, Starič A (2013) Orange: data mining toolbox in Python. *The Journal of Machine Learning Research* **14**, 2349–2353. doi:10.5555/2567709.2567736
- Drahota P, Knappová M, Kindlová H, Culká A, Majzlan J, Mihaljevič M, Rohovec J, Veselovský F, Fridrichová M, Jehlička J (2016) Mobility and attenuation of arsenic in sulfide-rich mining wastes from the Czech Republic. *Science of The Total Environment* **557–558**, 192–203. doi:10.1016/j.scitotenv.2016.03.079
- Fairbrother L, Etschmann B, Brugger J, Shapter J, Southam G, Reith F (2013) Biomineralization of gold in biofilms of *Cupriavidus metallidurans*. *Environmental Science & Technology* **47**, 2628–2635. doi:10.1021/es302381d
- Filippou D, Demopoulos GP (1997) Arsenic immobilization by controlled scorodite precipitation. *JOM* **49**, 52–55. doi:10.1007/s11837-997-0034-3
- Fleet ME, Burns PC (1990) Structure and twinning of cobaltite. *The Canadian Mineralogist* **28**, 719–723.
- Flores K, Turley RS, Valdes C, Ye Y, Cantu J, Hernandez-Viezcas JA, Parsons JG, Gardea-Torresdey JL (2021) Environmental applications and recent innovations in single particle inductively coupled plasma mass spectrometry (SP-ICP-MS). *Applied Spectroscopy Reviews* **56**, 1–26. doi:10.1080/05704928.2019.1694937
- Friedrich AJ, Luo Y, Catalano JG (2011) Trace element cycling through iron oxide minerals during redox-driven dynamic recrystallization. *Geology* **39**, 1083–1086. doi:10.1130/G32330.1
- Gao Y-P, Yang Y, Li L, Wei W-J, Xu H, Wang Q, Qiu Y-Q (2020) Quantitative detection of gold nanoparticles in soil and sediment. *Analytica Chimica Acta* **1110**, 72–81. doi:10.1016/j.aca.2020.03.005
- Geosciences Australia (2023) Scientific topics: critical minerals at Geoscience Australia. (Geosciences Australia, Australian Government) Available at <https://www.ga.gov.au/scientific-topics/minerals/critical-minerals>
- Ghodake G, Seo YD, Lee DS (2011) Hazardous phytotoxic nature of cobalt and zinc oxide nanoparticles assessed using *Allium cepa*. *Journal of Hazardous Materials* **186**, 952–955. doi:10.1016/j.jhazmat.2010.11.018
- Gonzalez de Vega R, Lockwood TE, Paton L, Schlatt L, Clases D (2023) Non-target analysis and characterisation of nanoparticles in spirits via single particle ICP-TOF-MS. *Journal of Analytical Atomic Spectrometry* **38**, 2656–2663. doi:10.1039/D3JA00253E
- Habjanič J, Jurič M, Popović J, Molčanov K, Pajič D (2014) A 3D oxalate-based network as a precursor for the CoMn₂O₄ spinel: synthesis and structural and magnetic studies. *Inorganic Chemistry* **53**, 9633–9643. doi:10.1021/ic501134y
- Huang Z (2023) The impact of new energy vehicle batteries on the natural environment and recycling method. In 'Proceedings of the 6th International Conference on Economic Management and Green Development. Applied Economics and Policy Studies', 6–12 August 2022, Stanford, CA, USA. (Eds X Li, C Yuan, J Kent) (Springer: Singapore) doi:10.1007/978-981-19-7826-5_8
- Iravani S, Varma RS (2020) Sustainable synthesis of cobalt and cobalt oxide nanoparticles and their catalytic and biomedical applications *Green Chemistry* **22**(9), 2643–2661. doi:10.1039/d0gc00885k

- Jambor J, Boyle R (1965) Moorhouseite and aplowite, new cobalt minerals from Walton, Nova Scotia. *The Canadian Mineralogist* **8**, 166–171.
- Kappler A, Bryce C, Mansor M, Lueder U, Byrne JM, Swanner ED (2021) An evolving view on biogeochemical cycling of iron. *Nature Reviews Microbiology* **19**, 360–374. doi:10.1038/s41579-020-00502-7
- Khan S, Ansari AA, Khan AA, Ahmad R, Al-Obaid O, Al-Kattan W (2015) In vitro evaluation of anticancer and antibacterial activities of cobalt oxide nanoparticles. *JBIC Journal of Biological Inorganic Chemistry* **20**, 1319–1326. doi:10.1007/s00775-015-1310-2
- Klopogge JT, Duong LV, Weier M, Martens WN (2006) Nondestructive identification of arsenic and cobalt minerals from Cobalt City, Ontario, Canada: arsenolite, erythrite, and spherocobaltite on parammelsbergite. *Applied Spectroscopy* **60**, 1293–1296. doi:10.1366/000370206778999148
- Leblanc M, Billaud P (1982) Cobalt arsenide orebodies related to an upper Proterozoic ophiolite; Bou Azzer (Morocco). *Economic Geology* **77**, 162–175. doi:10.2113/gsecongeo.77.1.162
- Lei Z, Chen X, Wang J, Huang Y, Du F, Yan Z (2022) Guite, the spinel-structured $\text{Co}^{2+}\text{Co}^{3+}_2\text{O}_4$, a new mineral from the Sicomines copper-cobalt mine, Democratic Republic of Congo. *Mineralogical Magazine* **86**, 346–353. doi:10.1180/mgm.2022.27
- Li H, Santos F, Butler K, Herndon E (2021) A critical review on the multiple roles of manganese in stabilizing and destabilizing soil organic matter. *Environmental Science & Technology* **55**(18), 12136–12152. doi:10.1021/acs.est.1c00299
- Llorca S, Monchoux P (1991) Supergene cobalt minerals from New Caledonia. *The Canadian Mineralogist* **29**, 149–161.
- Lockwood TE, Gonzalez de Vega R, Clases D (2021) An interactive Python-based data processing platform for single particle and single cell ICP-MS. *Journal of Analytical Atomic Spectrometry* **36**, 2536–2544. doi:10.1039/D1JA00297J
- Lockwood TE, Gonzalez de Vega R, Du Z, Schlatt L, Xu X, Clases D (2024) Strategies to enhance figures of merit in ICP-ToF-MS. *Journal of Analytical Atomic Spectrometry* **39**, 227–234. doi:10.1039/D3JA00288H
- Ma Q, Chen L, Li X, Wang M, Liu L (2023) Assessment of cobalt recycling potential and environmental impact in China from 1994 to 2020. *Environmental Science and Pollution Research International* **30**, 27469–27482. doi:10.1007/s11356-022-24040-2
- Majzlan J, Lalinska B, Chovan M, Blass U, Brecht B, Gottlicher J, Steininger R, Hug K, Ziegler S, Gescher J (2011) A mineralogical, geochemical, and microbiological assessment of the antimony- and arsenic-rich neutral mine drainage tailings near Pezinok, Slovakia. *American Mineralogist* **96**, 1–13. doi:10.2138/am.2011.3556
- Majzlan J, Drahotka P, Filippi M, Grevel K-D, Kahl W-A, Plášil J, Boerio-Goates J, Woodfield BF (2012) Thermodynamic properties of scorodite and parascorodite ($\text{FeAsO}_4 \cdot 2\text{H}_2\text{O}$), kaňkite ($\text{FeAsO}_4 \cdot 3.5\text{H}_2\text{O}$), and FeAsO_4 . *Hydrometallurgy* **117–118**, 47–56. doi:10.1016/j.hydromet.2012.02.002
- Mancini L, Eslava NA, Traverso M, Mathieux F (2021) Assessing impacts of responsible sourcing initiatives for cobalt: insights from a case study. *Resources Policy* **71**, 102015. doi:10.1016/j.resourpol.2021.102015
- McNulty BA, Jowitt SM (2021) Barriers to and uncertainties in understanding and quantifying global critical mineral and element supply. *iScience* **24**, 102809. doi:10.1016/j.isci.2021.102809
- Missen OP, Lausberg ER, Brugger J, Etschmann B, Mills SJ, Momma K, Ram R, Maruyama M, Fang X-Y, Melchiorre E, Ryan CG, Villalobos-Portillo EE, Castillo-Michel H, Nitta K, Sekizawa O, Shuster J, Sanyal SK, Friedrich A, Hunt S, Tsuru Y, Takahashi Y, Michibata U, Dwivedi S, Rea MAD (2022a) Natural nanoparticles of the critical element tellurium. *Journal of Hazardous Materials Letters* **3**, 100053. doi:10.1016/j.hazl.2022.100053
- Missen OP, Mills SJ, Villalobos-Portillo, EE (2022b) Understanding nanoscale cobalt biogeochemical cycling: a step towards minimizing the environmental cost of a critical battery metal in surface environments [Data set]. European Synchrotron Radiation Facility.
- Moradpoor H, Safaei M, Rezaei F, Golshah A, Jamshidy L, Hatam R, Abdullah RS (2019) Optimisation of cobalt oxide nanoparticles synthesis as bactericidal agents. *Open Access Macedonian Journal of Medical Sciences* **7**(17), 2757–2762. doi:10.3889/oamjms.2019.747
- Mozhayeva D, Engelhard C (2020) A critical review of single particle inductively coupled plasma mass spectrometry – a step towards an ideal method for nanomaterial characterization. *Journal of Analytical Atomic Spectrometry* **35**, 1740–1783. doi:10.1039/C9JA00206E
- Mumba-Kankolongo A, Banza Lubaba Nkulu C, Mwitwa J, Kampemba FM, Mulele Nabuyanda M (2022) Impacts of trace metals pollution of water, food crops, and ambient air on population health in Zambia and the DR Congo. *Journal of Environmental and Public Health* **2022**, 4515115. doi:10.1155/2022/4515115
- Musa Obadia P, Kayembe-Kitenge T, Haufroid V, Banza Lubaba Nkulu C, Nemery B (2018) Preeclampsia and blood lead (and other metals) in Lubumbashi, DR Congo. *Environmental Research* **167**, 468–471. doi:10.1016/j.envres.2018.07.032
- Nagashima M, Morishita Y, Imoto Y, Imaoka T (2021) Ore and skarn mineralogy of the Eboshi deposit of the Naganobori copper mine, Yamaguchi, Japan. *Journal of Mineralogical and Petrological Sciences* **116**(1), 26–44. doi:10.2465/jmps.200818
- Nansai K, Nakajima K, Kagawa S, Kondo Y, Suh S, Shigetomi Y, Oshita Y (2014) Global flows of critical metals necessary for low-carbon technologies: the case of neodymium, cobalt, and platinum. *Environmental Science & Technology* **48**, 1391–1400. doi:10.1021/es4033452
- Nair GM, Sajini T, Mathew B (2022) Advanced green approaches for metal and metal oxide nanoparticles synthesis and their environmental applications *Talanta Open* **5**, 100080. doi:10.1016/j.talo.2021.100080
- Newsome L, Solano Arguedas A, Coker VS, Boothman C, Lloyd JR (2020) Manganese and cobalt redox cycling in laterites; biogeochemical and bioprocessing implications. *Chemical Geology* **531**, 119330. doi:10.1016/j.chemgeo.2019.119330
- Pell R, Tijsseling L, Goodenough K, Wall F, Dehaine Q, Grant A, Deak D, Yan X, Whattoff P (2021) Towards sustainable extraction of technology materials through integrated approaches. *Nature Reviews Earth & Environment* **2**, 665–679. doi:10.1038/s43017-021-00211-6
- Reith F, Fairbrother L, Nolze G, Wilhelmi O, Clode PL, Gregg A, Parsons JE, Wakelin SA, Pring A, Hough R, Southam G, Brugger J (2010) Nanoparticle factories: biofilms hold the key to gold dispersion and nugget formation. *Geology* **38**, 843–846. doi:10.1130/G31052.1
- Reith F, Brugger J, Zammit CM, Gregg AL, Goldfarb KC, Andersen GL, DeSantis TZ, Piceno YM, Brodie EL, Lu Z, He Z, Zhou J, Wakelin SA (2012) Influence of geogenic factors on microbial communities in metallogenic Australian soils. *The ISME Journal* **6**, 2107–2118. doi:10.1038/ismej.2012.48
- Schumer BN, Andrade MB, Evans SH, Downs RT (2017) A new formula and crystal structure for nickelskutterudite, (Ni, Co, Fe) As₃, and occupancy of the icosahedral cation site in the skutterudite group. *American Mineralogist* **102**, 205–209. doi:10.2138/am-2017-5615
- Schwartz FW, Lee S, Darrah TH (2021) A review of health issues related to child labor and violence within artisanal and small-scale mining. *GeoHealth* **5**, e2020GH000326. doi:10.1029/2020GH000325
- Simanova AA, Peña J (2015) Time-resolved investigation of cobalt oxidation by Mn(III)-rich $\delta\text{-MnO}_2$ using quick X-ray absorption spectroscopy. *Environmental Science & Technology* **49**, 10867–10876. doi:10.1021/acs.est.5b01088
- Solé VA, Papillon E, Cotte M, Walter P, Susini J (2007) A multiplatform code for the analysis of energy-dispersive X-ray fluorescence spectra. *Spectrochimica Acta – B. Atomic Spectroscopy* **62**, 63–68. doi:10.1016/j.sab.2006.12.002
- Subías I, Fanlo I, Hajjar Z, Gervilla F, Billström K (2022) Isotopic constraints on the age and source of ore-forming fluids of the Bou Azzer arsenide ores (Morocco). *Ore Geology Reviews* **143**, 104769. doi:10.1016/j.oregeorev.2022.104769
- Sundararaju S, Arumugam M, Bhuyar P (2020) *Microbacterium* sp. MRS-1, a potential bacterium for cobalt reduction and synthesis of less/non-toxic cobalt oxide nanoparticles (Co_3O_4). *Beni-Suef University Journal of Basic and Applied Sciences* **9**, 44. doi:10.1186/s43088-020-00070-y
- Tagliabue A, Hawco NJ, Bundy RM, Landing WM, Milne A, Morton PL, Saito MA (2018) The role of external inputs and internal cycling in shaping the global ocean cobalt distribution: insights from the first cobalt biogeochemical model. *Global Biogeochemical Cycles* **32**, 594–616. doi:10.1002/2017GB005830

- Tanaka K, Yu Q, Sasaki K, Ohnuki T (2013) Cobalt(II) oxidation by biogenic Mn oxide produced by *Pseudomonas* sp. strain NGY-1. *Geomicrobiology Journal* 30, 874–885. doi:10.1080/01490451.2013.791352
- Tharaud M, Schlatt L, Shaw P, Benedetti MF (2022) Nanoparticle identification using single particle ICP-ToF-MS acquisition coupled to cluster analysis. From engineered to natural nanoparticles. *Journal of Analytical Atomic Spectrometry* 37, 2042–2052. doi:10.1039/D2JA00116K
- Toplak M, Birarda G, Read S, Sandt C, Rosendahl SM, Vaccari L, Demšar J, Borondics F (2017) Infrared orange: connecting hyperspectral data with machine learning. *Synchrotron Radiation News* 30, 40–45. doi:10.1080/08940886.2017.1338424
- Vafeas NA, Bignaut LC, Viljoen KS (2019) Arsenic-bearing manganese ore of the Mukulu Enrichment in the Kalahari Manganese Field, South Africa: a new discrimination scheme for Kalahari manganese ore. *Ore Geology Reviews* 115, 103146. doi:10.1016/j.oregeorev.2019.103146
- Watari T, Nansai K, Nakajima K (2020) Review of critical metal dynamics to 2050 for 48 elements. *Resources, Conservation and Recycling* 155, 104669. doi:10.1016/j.resconrec.2019.104669
- Wildner M, Giester G, Lengauer CL, McCammon CA (1996) Structure and crystal chemistry of vivianite-type compounds: crystal structures of erythrite and annabergite with a Mössbauer study of erythrite. *European Journal of Mineralogy* 8, 187–192. doi:10.1127/ejm/8/1/0187
- Whitworth AJ, Forbes E, Verster I, Jokovic V, Awatey B, Parbhakar-Fox A (2022) Review on advances in mineral processing technologies suitable for critical metal recovery from mining and processing wastes *Cleaner Engineering and Technology* 7, 100451. doi:10.1016/j.clet.2022.100451

Data availability. Compiled SP ICP-MS and bulk Co and Mn data presented in this paper may be obtained from Supplementary Table S1. Synchrotron data are available from [Missen et al. \(2022b\)](#).

Conflicts of interest. The authors declare that they have no conflicts of interest.

Declaration of funding. S. J. Mills gratefully acknowledges Glenda and Greg Lewin AM and the Geological Society of Australia (GSA) for funding to support this project through Museums Victoria. This study was financed in part by the Coordenação de Aperfeiçoamento de Pessoa de Nível Superior – Brazil (CAPES) – Financed Code 001. O. P. Missen acknowledges support from the project ‘Building capacity in Regional Australia to enhance Australia’s Economy through research, training, and environmentally sustainable production of critical metals’, supported by the Australian Government Department of Education.

Acknowledgements. The authors thank three anonymous reviewers for their insightful comments that improved the initial manuscript, and editor Dr Kevin Wilkinson for handling the paper. The authors are grateful to NT Minerals Ltd (in particular Mike Cowin, Chris Rutherford and Brent Simpson) and Cobalt Blue Holdings Ltd (in particular Heath Porteous) for allowing access to their sites to conduct the sampling campaign. They also thank Costas Constantinides (Mount Isa, Queensland) and Allan Pring, Peter Elliott (University of Adelaide, Australia) and John Toma (South Australian Museum, Adelaide, Australia) for assistance with fieldwork planning. Finally, the authors thank Joël Brugger and Barbara Etschmann (Monash University) for providing access to laboratory facilities and reagents, Junnel Alegado (Monash University) for petrographic services and Oskar Lindenmayer (Museums Victoria) for assistance with specimen registration.

Author affiliations

^AGeosciences, Museums Victoria, GPO Box 666, Melbourne, Vic. 3001, Australia.

^BCentre for Ore Deposit and Earth Sciences, University of Tasmania, Hobart, Tas. 7001, Australia.

^CInstitute of Chemistry, University of Graz, Graz, AT-8010, Austria.

^DDepartamento de Química, Campus Trindade, Universidade Federal de Santa Catarina, Florianópolis, SC 88040-900, Brazil.

^EEuropean Synchrotron Radiation Facility, Grenoble, Cedex 9, F-38043 France.

^FHyphenated Mass Spectrometry Lab, University of Technology Sydney, NSW 2007, Australia.

^GPresent address: ALBA Synchrotron, Cerdanyola del Valles, Barcelona E-08290, Spain.